The Meteoritical Society

Meteoritics & Planetary Science 52, Nr 7, 1505–1522 (2017)
doi: 10.1111/maps.12913

Hypervelocity impacts into ice-topped layered targets: Investigating the effects of ice crust thickness and subsurface density on crater morphology

Kathryn H. HARRISS* and Mark J. BURCHELL

Centre for Astrophysics and Planetary Science, School of Physical Sciences, University of Kent, Canterbury, Kent CT2 7NH, UK
*Corresponding author. E-mail: K.Harriss@kent.ac.uk

(Received 18 March 2016; revision accepted 15 May 2017)

Abstract–Many bodies in the outer solar system are theorized to have an ice shell with a different subsurface material below, be it chondritic, regolith, or a subsurface ocean. This layering can have a significant influence on the morphology of impact craters. Accordingly, we have undertaken laboratory hypervelocity impact experiments on a range of multilayered targets, with interiors of water, sand, and basalt. Impact experiments were undertaken using impact speeds in the range of 0.8–5.3 km s^{-1}, a 1.5 mm Al ball bearing projectile, and an impact incidence of 45°. The surface ice crust had a thickness between 5 and 50 mm, i.e., some 3–30 times the projectile diameter. The thickness of the ice crust as well as the nature of the subsurface layer (liquid, well consolidated, etc.) have a marked effect on the morphology of the resulting impact crater, with thicker ice producing a larger crater diameter (at a given impact velocity), and the crater diameter scaling with impact speed to the power 0.72 for semi-infinite ice, but with 0.37 for thin ice. The density of the subsurface material changes the structure of the crater, with flat crater floors if there is a dense, well-consolidated subsurface layer (basalt) or steep, narrow craters if there is a less cohesive subsurface (sand). The associated faulting in the ice surface is also dependent on ice thickness and the substrate material. We find that the ice layer (in impacts at 5 km s^{-1}) is effectively semi-infinite if its thickness is more than 15.5 times the projectile diameter. Below this, the crater diameter is reduced by 4% for each reduction in ice layer thickness equal to the impactor diameter. Crater depth is also affected. In the ice thickness region, 7–15.5 times the projectile diameter, the crater shape in the ice is modified even when the subsurface layer is not penetrated. For ice thicknesses, <7 times the projectile diameter, the ice layer is breached, but the nature of the resulting crater depends heavily on the subsurface material. If the subsurface is noncohesive (loose) material, a crater forms in it. If it is dense, well-consolidated basalt, no crater forms in the exposed subsurface layer.

Highlights

- Hypervelocity impacts into ice.
- Multilayered ice targets.
- Impact cratering on Europa.

INTRODUCTION

Impact craters are a common geological feature in the solar system (Hartmann 1977). The study of these features, along with an understanding of the cratering mechanics that form them, can aid in our understanding of the internal structure and evolutionary history of the different planetary bodies and satellites (Barlow 2015). Ice surfaces are numerous throughout the solar system, including polar caps and permafrost of the terrestrial planets Earth and Mars (Tanaka and Scott 1987), and even in constant shadowed regions on the Moon (Hayne et al. 2015) and Mercury (Chabot et al. 2012). Permafrost is theorized to exist in the subsurface of Mars and extend down to a depth of at least 1 km (Tanaka and Scott [1987] and references therein). Indeed, in the polar regions, the Martian cryosphere may extend to around 6 km below the Martian surface (Clifford et al. 2010). This means that impacts on Mars are not just into regolith-covered basement rock, but potentially

into regolith infused with water ice above an igneous subsurface lithology.

Beyond the solar system frost line, outside of which water and other volatiles begin to condense, it is theorized that icy material could make up to 50% of mass of material that condensed from the solar nebula (Prockter 2005). This material includes the icy moons of the gas giant planets, asteroids, comets, and dwarf planets. Comets and other trans-Neptuniun objects, such as Pluto and Charon, are remnants of the solar system formation as the outer reaches of the nebular would have been sufficiently cold to allow for rapid accretion of ices onto rocky cores (Prockter 2005). The moons of the gas giants would have condensed from the proto-gas giant planets material disk to form small icy and rocky bodies. In this case, the proportion of rock and ice varies with distance from the parent planet. For example, the rocky, and volcanically active, moon Io (density some 3.5 g/cc) is close to Jupiter, while the undifferentiated icy moon Callisto (density some 1.8 g/cc and which has the oldest most cratered surface) is some four times farther away, indicating the position of the frost line of the Jupiter proto disk. The bodies that form do not have to be homogeneous, i.e., their interiors do not have to be the same as the surface. Thus, the surface ice layer may overlay a different interior, such as a rocky substrate or a liquid ocean.

Such a dynamic and large range in the types of ice surfaces in the solar system has led to a variety of topographical features being formed and observed in the ice on different bodies. Indeed, a range of features can even exist on one type of such body. For example, the three ice-dominated Galilean moons of Jupiter (Europa, Callisto, and Ganymede) show different surface features as the orbital distance from Jupiter increases. Callisto has an old impact scarred crust, compared to the dynamic and sometimes smooth surface of Europa. The geological features on the surface of Europa include the large multiringed shallow impact craters of Tyre and Callanish (Fig. 1), thought to have formed as a result of the impact of bodies between 2 and 4 km in diameter penetrating the ice crust (Zahnle et al. 2003). A predominant geological feature along with these large impact craters is chaos terrain. This is characterized by broad areas where large blocks of original terrain occur in a structureless and hummocky matrix, with a texture that resembles detached icebergs left to drift before the whole region refreezes. Currently, these areas are thought to be the result of internal heating causing melting of the ice crust in a specific area, similar to a hot spot on the Earth's surface (Ivanov et al. 2011). An alternative idea, however, is that these areas are the result of impacts involving full crustal penetration (Cox et al. 2008), causing the breakup of the surface producing the rafts of the original ice terrain, which are then refrozen in place once the external heat of the impact dissipates. Therefore, chaos areas may be a hitherto unrecognized record of full crustal penetration by an impactor (Cox et al. 2008; Cox and Bauer 2015). In general, the preservation of layers of different material in a target may influence the outcome of an impact event. This alternation can change the development of the growth of the crater or the subsequent modification of the impact site on longer time scales resulting in an altered morphology (Head 1976; Grieve 1987).

Orbital missions studying the Jovian and Saturnian moons, including Voyager 1 and 2, Galileo, and Cassini, have provided evidence that on the icy moons of Europa, Ganymede, Callisto, and Enceladus, an ice crust may lie above a subsurface ocean based upon thermal analyses and surface observations (Cassen et al. 1982; Squyres et al. 1983; Ross and Schubert 1987; Schenk and McKinnon 1989; Carr et al. 1998; Hoppa et al. 1999; Pappalardo et al. 1999; Turtle and Pierazzo 2001; Schenk and Turtle 2009; Walker and Schmidt 2015). The variation in subsurface material at shallow depths (<100 km) will have a major effect on the cratering mechanics during large hypervelocity impacts on these moons, or similar ice-covered regions on other bodies. As the pressure waves produced by the impact passes through the different materials, the speed and angles of the pressure and release waves will change, resulting in an alteration of the crater produced. Such variation in the cratering mechanics will be linked to the thickness of the individual ice crust and the density of the subsurface material, as well as other variables (Head 1976; Grieve 1987).

The study of impact craters and cratering in layered targets is a dynamic area of research due to the complexity of the number and variety of the target types involved. Many studies of impact craters have discussed variations in morphology as dependence on the underlying layered material. Stickle and Schultz (2013) discussed the lack of distinctive shock features at the Rock Elm impact structure (Wisconsin) as a result of low-impedance surface layers over high-impedance bedrock, which affects the shock effects in the substrate. This was confirmed by laboratory and computational modeling showing how a nonhomogenous target produces distinct crater morphology (Stickle and Schultz 2013). Impacts into a layered target with variation in material strength between sedimentary and crystalline layers were undertaken by Collins and Wünnemann (2005), investigating the formation of the Chesapeake Bay impact, who found that the distinctive features of this impact crater are due to the layered target properties. Wünnemann et al. (2005) also

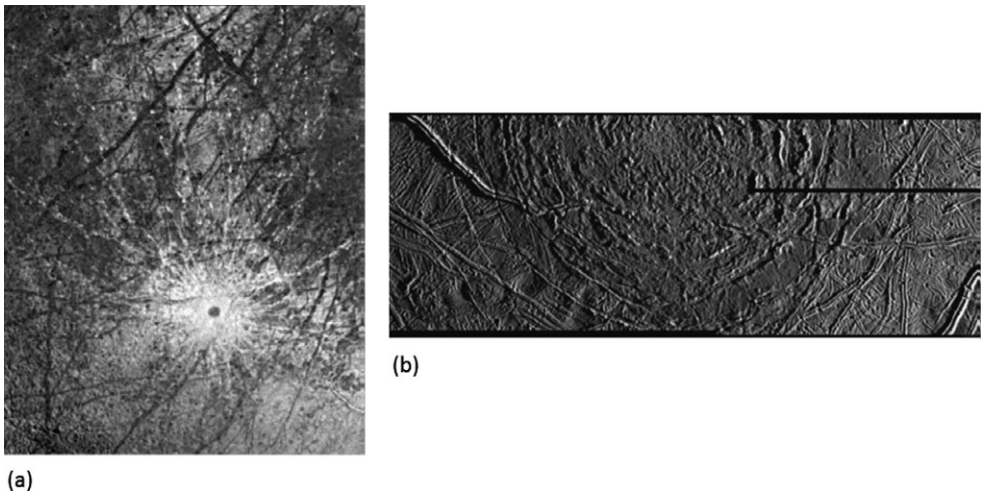

Fig. 1. Images from the Galileo Mission of craters on Europa including (a) 1.2 km/pixel coverage showing the Pwyll's ray system. 1300 by 1700 km. North is up. (Moore et al. 2001). b) Southern portion of Callanish (16°S, 334 °wn) 120 m/pixel. North is up (Moore et al. 2001).

concluded that the final shape of the Ries crater is sensitive to the constitutive properties of the target rock with sedimentary and crystalline layers. These studies and others (e.g., Pike 1980; Pierazzo and Melosh 1999; Kenkmann et al. 2005) all provide evidence for the effect of heterogeneous targets on crater morphology. A comparative study by Collins et al. (2008) compared the observations and computation models of three terrestrial craters in order to understand the effects of target properties on the cratering processes. That work concluded that the structural differences in crater morphology are related to the thickness of the preimpact sedimentary layer with one major conclusion being that for constant impact energy, the transient and final crater diameters increase with increasing sediment thickness. However, there has been little work investigating the effect of an ice layer above a substrate of other materials.

Hypervelocity impact experiments onto ice targets have been previously studied by a number of groups investigating various aspects of the impact process. Impact cratering on water ice has been previously studied by, among others, Croft (1981), Kadono and Fujiwara (1996), Burchell et al. (2001), Grey et al. (2001, 2002), Shrine et al. (2002), Giacomuzzo et al. (2007), and Miljkovic et al. (2011). Most of these previous studies focused on solid water ice or porous water ice targets. Impact craters in other ices, such as CO_2 (Burchell et al. 1998, 2005) and NH_3 (Grey and Burchell 2004), have also been studied. Models of these laboratory-scale impact cratering events often fail to account for the late-stage spallation which widens the initial impact crater formed in ice. However, Fendyke et al. (2013) showed that it is possible to simulate laboratory-scale hypervelocity impacts into thick water ice targets and Bray et al. (2014) showed that layered targets can also be simulated. Hypervelocity impact disruption experiments on icy targets have also been reported by, for example, Arakawa (1999), Arakawa et al. (2002), and Leliwa-Kopystynski et al. (2008). The role of layering in icy targets was considered in low-speed impacts (at up to 0.6 km s^{-1}) by Arakawa et al. (2000) who found that having ice-rich surface layers clearly influenced crater development.

When considering impacts in layered surfaces with an ice crust, the thickness of the ice crust and density of the subsurface material provide additional considerations for the cratering mechanics, as the pressure waves from the impact must travel through different mediums with an impedance mismatch between them. Modeling work undertaken by Senft and Stewart (2008), for example, investigated the effect that ice layers within and above a planetary surface have on impact cratering under Martian conditions. They concluded that the presence of ice could be used to explain some of the unusual features within craters observed on the Martian surface, meaning that an icy layer either within, or above, the subsurface material leads to variation in the final crater morphology. This can aid in identifying areas on Mars which have, or have previously had, near-surface ice layers.

In this work, we present the results of a series of impact experiments onto three types of multilayered targets (1) ice over water, (2) ice over sand, and (3) ice over basalt. This is to simulate multiple possible surfaces that exist in the solar system, where ice overlays a different subsurface material. The ice crust thickness for each target ranged from 5 to 50 mm, with

a consistent impact speed of 5 km s^{-1}. In addition, we have investigated the effect of changes in impact speeds (1, 3, and 5 km s^{-1}) on differing ice thicknesses above a sand subsurface. For comparison, reference impacts into a solid (semi-infinite) ice target were also undertaken at 1, 3, and 5 km s^{-1}.

EXPERIMENTAL METHOD

The impact experiments were undertaken using the two-stage light-gas gun at the University of Kent (Burchell et al. 1999). The projectile for each shot was a 1.5 mm Al sphere loaded into a nylon sabot which was discarded in flight. The target chamber was evacuated to typically 50 mbar before each shot so that the projectile does not slow in flight.

Working with ice in a nonfrozen environment means that we have to take steps so that the target does not melt during the experiment. The targets are placed into the chamber with a surface temperature of ~−23 °C (mean −22.8°C) for ~15 min while the chamber reaches 50 mbar; during this time, the temperature of the ice rises by approximately 7.4 °C, meaning the temperature of the surface ice at the point of impact was approximately −15.4 °C.

Type (a) Targets: Ice Over Water

Type (a) targets were formed by freezing a cylinder of water from the topdown for a set period of time to achieve the ice thickness over water required for each shot. The water was placed into a cylindrical tub, 210 mm wide by 80 mm deep, and insulated on all sides with the top surface open to a −25 °C environment. The time to produce 10 mm thickness of surface ice was typically 4 h. To minimize the possibility of impurities and bubbles forming, producing weak areas within the ice, 18 MΩ cm water was used, which was initially boiled, then cooled to 4 °C and finally siphoned into the cylinder. This method was a development of the method of producing clear (flaw free) ice reported by Grey et al. (2001).

Type (b) Targets: Ice Over Sand

For targets type (b), the sand was saturated until water pooled on the surface. The whole target was placed into the same freezing technique described above resulting in only the freezing of the water above the sand creating the ice crust. The sand used had a grain size between 0.1 and 0.3 mm, and formed a subsurface layer 50–60 mm deep. The maximum ice thickness used was 30 mm, giving a total maximum depth of 80–90 mm. The sand used was basic builder sand with a density of 1.5 g cm^{-3} with a porosity of ~20%.

Type (c) Targets: Ice Over Basalt

For targets type (c), the ice crust was produced beforehand using a similar method as that described above in the Type (a) Targets: Ice Over Water section. The water was poured into a 200 mm diameter silicon mold and placed into the insulating cover. The water was left to freeze for the time required to form the required ice thickness. The ice was then removed intact from the silicon mold and stored within the −25°C freezer, wrapped in a plastic sheet to prevent frosting. The basalt subsurface was a basaltic cylinder of 60 mm diameter and extended to a depth of 70 mm. Given that the basalt had a diameter less than the ice, the basalt column was surrounded by an annulus of sand of the same depth as the basalt. The ice crust was then frozen to the surface of the basalt by freezing the basalt and then providing a layer of water to freeze the ice layer to the surface of the basalt, such that the ice over basalt region was centered at the point of impact. The basalt was obtained from the tertiary basalt formation on the Isle of Skye with a density of 2.8 g cm^{-3}. For one shot, a second basalt type target was made using a larger basalt block 20 cm × 10 cm. This block was frozen with a −25 °C environment and a premade ice layer was added to top of the basalt and frozen in contact with the basalt.

Type (d) Targets: Solid Ice

As a standard homogenous ice target for comparison shots, a solid ice target was formed using the same method as described in the Type (a) Targets: Ice Over Water section. A freezing time of 10 h formed an ice cylinder of 210 diameter and 80 mm depth.

Mounting in the Gun

After manufacture, each target type was placed into the target chamber at an angle of 45°, to the horizontal (the Kent gun fires horizontally). An incidence of 45° was chosen as this is the mean impact angle for solar system impacts (e.g., see Pierazzo and Melosh 2000). A stainless steel ring, cooled to a temperature of −140 °C, was placed around the target. This prevented any small leakage of water through gaps in the edges of the target (where the ice layer meets the mold), by freezing the escaping water upon contact forming a blockage. Once the target was placed into the target chamber, the chamber was evacuated to a pressure of 50 mbar and the shot was carried out. After the shot was completed, the target was removed and the resulting impact crater was measured using calipers. Measurement of the crater morphology was undertaken using four measurements

of the spall diameter (spread evenly around the circumference of the crater), and the mean value was recorded with the standard deviation of the values. Using the spall diameter is typical when working with ice, as spall fragments melt too quickly to allow for reassembly of the crater; this is similar to the method by other studies of crater in ice (e.g., Shrine et al. 2002). The diameter of the central pit in a crater (if present) was measured similarly. Spall is a feature of craters in brittle materials in laboratory (strength dominated)-scale experiments. However at planetary scale, in a gravity-dominated regime, we do not expect to see spallation and therefore craters may be slightly smaller than those predicted from extrapolated or scaled values from laboratory experiments which feature spallation.

In addition, a depth profile was taken along one axis of the crater (passing through the deepest point at the center). The depth at the deepest point was measured in this way accurate to 0.5 mm, and observations of any faulting in the ice were recorded along with multiple images (Figs. 2–6). The speed for each shot was measured using a pair of laser light focused onto photodiodes. Interruption of the light by the projectile caused a change in the laser output, the timing of which can be measured accurately. Having two such stations, a known distance apart allows the speed of the projectile to be calculated in each shot to an accuracy of better than ±1%. The results of 31 shots are reported here.

RESULTS

The impact parameters for each shot and characteristics of the resulting craters are given in Table 1. The results presented below describe the craters formed in the various target types. Images of the crater produced for all target types and impact velocities investigated are shown in Figs. 2–6.

Ice Over Water at 5 km s^{-1}

Eight experiments were observed in this category; examples of the craters formed in the ice above water target are shown in Fig. 2. The mean impact speed was 5.14 ± 0.16 km s^{-1}, with all impacts in the speed range 4.9–5.4 km s^{-1}. The thickness of the surface ice layer ranged between 10 mm, which when normalized to projectile diameter of 1.5 mm is 6.7 (normalized ice thickness is displayed in brackets after the ice thickness value), and 50 mm (33.3) (see Table 1). Where the ice layer was penetrated, no depth profile could be conducted as no crater profile could remain in the subsurface water media.

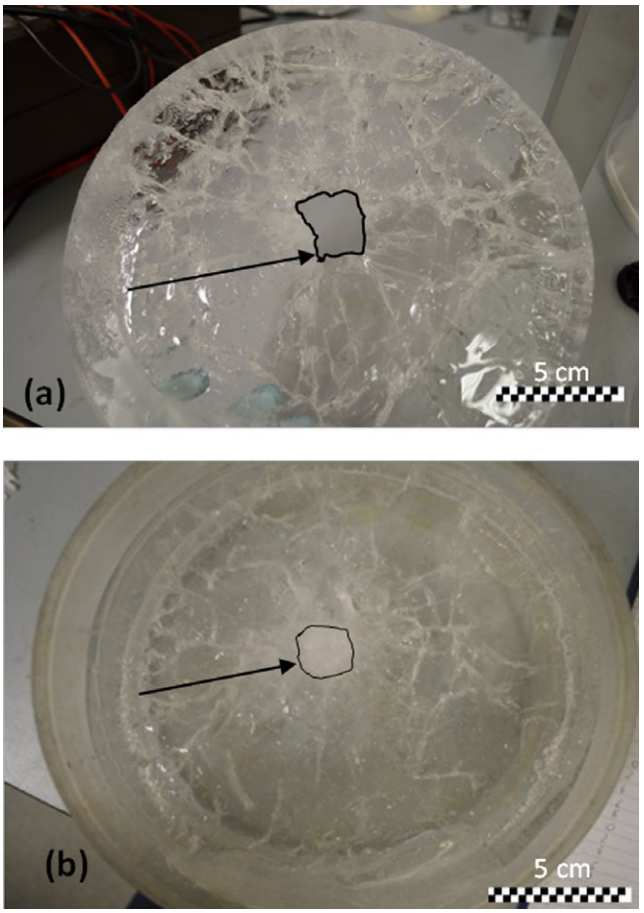

Fig. 2. Images of craters formed by impacts in type (a) targets (ice over water). The target diameter was 210 mm. The impact speed in each case was ~5 km s^{-1}. Radial and lateral fractures are also present in the ice in all cases. a) G111214#2—10 mm ice thickness showing a penetrative impact. b) G040315#4—20 mm ice thickness showing a nonpenetrative impact. Crater outline is shown by the arrow and the black outline. (Color figure can be viewed at wileyonlinelibrary.com.)

5–19 mm Ice Thickness (Penetrative Impacts)

The shot at the 10 mm (6.7) ice crust produced an elongated hole penetrating the ice crust into the water below. Around the rim of the steep-sided crater were numerous radial cracks up to 10 mm in length producing white crushed ice (Fig. 2a). Ten additional radial fractures stretched away from the point of impact, becoming interconnected with lateral joining faults traveling perpendicular to the radial fractures. Toward the edge of the target, two circular fractures (one complete and one partial) formed about 50 mm away from the edge of the target. Such features have been previously observed in other brittle targets including glass (Burchell and Grey 2001).

Impacts into the four targets with an ice thickness between 12 mm (8.1) and 16 mm (10.5) produced similar types of craters to that observed for the 10 mm

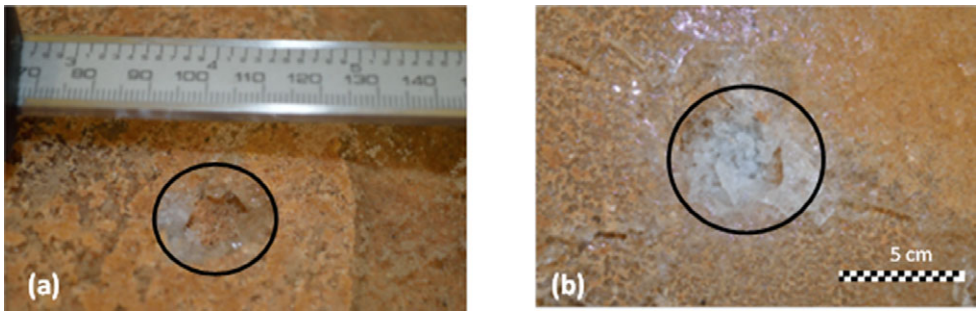

Fig. 3. Images of the penetrative impacts into a target of ice over saturated sand at impact speed of (a) 1 km s^{-1} (S110914#2) and (b) 5 km s^{-1} (G150814#2) with a thickness of <10 mm (8 mm and 10 mm, respectively). (Color figure can be viewed at wileyonlinelibrary.com.)

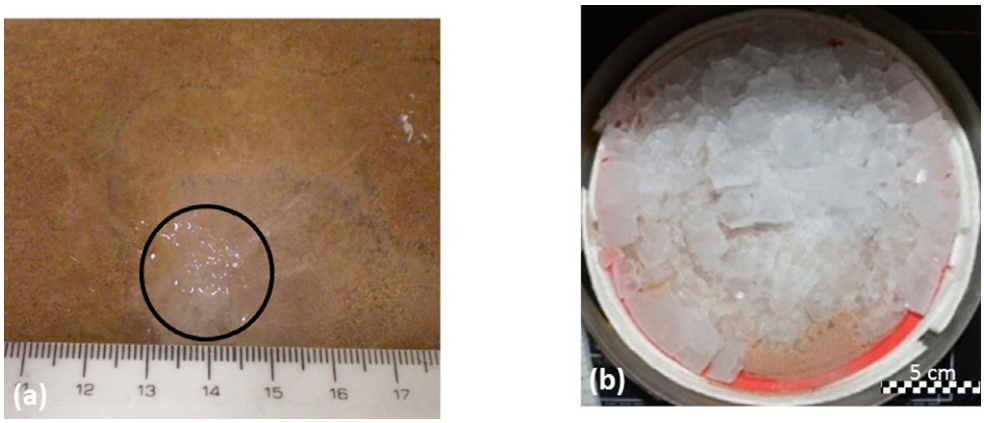

Fig. 4. Examples of nonpenetrative impacts into target of ice over saturated sand at impact speed of (a) ~1 km s^{-1} (S250914#2) and (b) ~5 km s^{-1} (G040315#3). Ice thickness of 10.1 mm and 16.1 mm, respectively. (Color figure can be viewed at wileyonlinelibrary.com.)

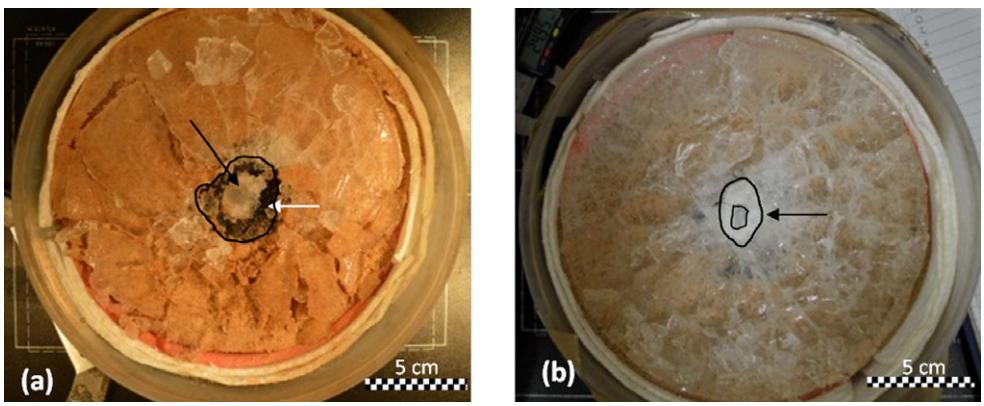

Fig. 5. Images of the craters formed within targets of ice over basalt with an impact speed of 5 km s^{-1}. The diameter of each target is 210 mm. The crushed ice at the center of the impact is shown by the black arrow, exposing the subsurface basalt is shown by the white arrow. a) G030215#1—10 mm ice thickness. b) G280515#2—near 20 mm ice thickness. (Color figure can be viewed at wileyonlinelibrary.com.)

(6.7) ice thickness, with the exception that the size of the penetrating "bullet" hole was significantly larger (Fig. 2b). Other features of the crater remained similar to that in the thinner ice crust, with numerous short radial fractures forming around the crater edge and longer radial fractures stretching away (Fig. 2a). Circular fractures were again observed about 50 mm away from the edge of the target, and one circular

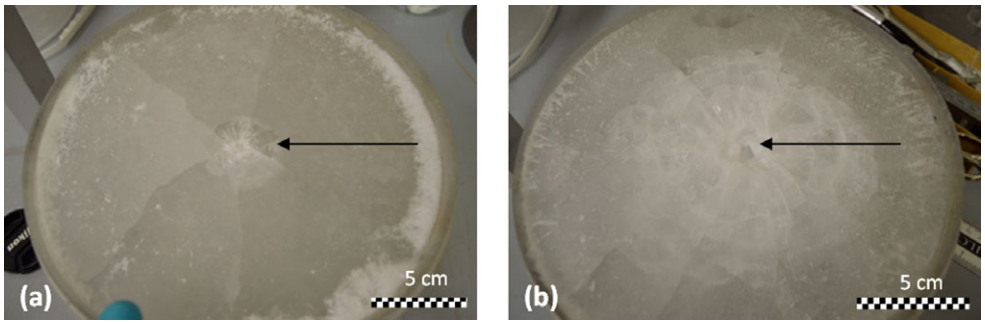

Fig. 6. Images of the craters produced in the solid ice targets with a thickness of 80 mm and diameter of 210 mm with the point of impact shown (black arrows). The impact speed is shown varying from 1 to 5 km s^{-1}. a) S031013#1—1 km s^{-1} impact speed. b) G19091#1—5 km s^{-1} impact speed. (Color figure can be viewed at wileyonlinelibrary.com.)

fracture was observed 30 mm away from the crater edge.

20–50 mm Ice Thickness (Nonpenetrative Impacts)

Nonpenetration of the ice layer was observed for ice thicknesses above 20 mm (13.3). At an ice thickness of 20 mm (13.3), a large crater was formed with a mean diameter of 54.9 ± 5.8 mm and a maximum depth of 5.3 mm. Numerous small radial faults were observed around the craters, in addition to seven larger radial fractures and one partial circular fracture near the edge of the target. The central pit of the crater had the distinctive white appearance of finely crushed and highly fractured ice. An impact into ice thickness of 13.5 mm (9.0) also produced a nonpenetrative impact which appears to be an anomaly, with a shallow (6.1 mm) narrow (35.5 mm) crater being formed. No explanation was found for this.

With an ice thickness of 50 mm (33.3), a large crater was observed with a mean diameter of 52.9 ± 5.1 mm. This diameter was comparable with the crater in the 20 mm (13.3) thick ice, suggesting the smaller depth of ice is sufficient to permit the full crater to form. There are few small fractures along the edge of the crater, and about 10 radial fractures extended the length of the target away from the crater edge. One circular fracture was observed 60 mm away from the center of the crater. The crater depth was 15.1 mm, much larger than in the 20 mm (13.3) thick ice, and equivalent to the depth of impact at 4.9 km s^{-1} into a solid ice target, although, however, the crater diameter does differ (see later).

Ice Over Sand

This target type was used to investigate the changes in crater morphology with a similar ice thickness at each of the three impact speeds, 1, 3, and 5 km s^{-1}. At the higher speed of 5 km s^{-1}, the data can be compared with the crater morphologies produced by impact on the other target types (i.e., different subsurface densities). The discussion is divided into impacts that produced penetrative and nonpenetrative impact craters. The effect of impact speed on crater morphology is discussed further in the Variation in Crater Morphology With Impact Speed section.

(a) Penetrative Impact

For speeds of ~1 km s^{-1} (mean speed was 0.92 ± 0.1 km s^{-1}), penetration of the ice crust was observed for ice thicknesses of 5 mm (3.3) and 10 (6.7) mm (Fig. 3), with the Al projectile being recovered from the sand material below with little to no obvious modification. After penetration of the ice, a crater was formed in the sand below the penetrated ice crust, such craters being relatively deep and narrow (Table 1). Note that in Table 1, the crater depth is the total depth below the surface of the ice layer. Ice from the point of impact was crushed, producing white thin layers of the ice crust within the subsurface sand. Radial cracks in the ice surface were present.

At the impact speed of ~3 km s^{-1} (mean speed was 3.16 ± 0.09 km s^{-1}), a penetrative bullet hole impact is produced in ice thicknesses of 8 mm (5.3) and 13.8 mm (9.2). The impact in the 13.8 mm (9.2) ice crust penetrated the ice and formed a bowl-shaped crater of shattered ice within the sand material below of diameter 25.9 ± 1.7 cm; the mean diameter of the crater in the icy surface was 25.4 ± 6.0 mm.

Five of the six shots that were completed at a speed of ~5 km s^{-1} (mean speed was 5.15 ± 0.17 km s^{-1}), resulted in penetrative impacts with a range of ice thicknesses from 4.3 mm (2.9) to 16.1 mm (10.7). The penetrative impact craters were steep-sided with crushed ice mixed with the subsurface sand in the base of the crater. Numerous short radial fractures were formed around the edges of the deep side crater and the mean size of the crater increases with ice thickness from 28.0 ± 2.7 mm for 8 mm (5.3) ice thickness to

Table 1. Data for the impact experiments within ice surface targets, divided into subsurface.

Target type (see text)	Shot #	Ice thickness (mm)	Ice thickness/ projectile diameter	Velocity (m s^{1})	Pressure* (GPa)	Mean crater diameter (mm)	Standard deviation (lσ)	Mean pit diameter (mm)	Standard deviation (lσ)	Depth (mm)	Depth/ thickness	Depth/ diameter	Error
Type A	G111214#2	10.0	6.7	5080	25.1	25.4	4.9	n/a	n/a	n/a	n/a	n/a	n/a
water	G201114#2	12.2	8.1	5170	25.8	43.9	4.6	20.6	2.4	n/a	n/a	n/a	n/a
	G061016#l	13.5	9.0	5030	24.7	35.5	1.5	n/a	n/a	6.1	0.5	0.2	0.03
	G121114#l	14.2	9.5	5380	27.4	44.9	5.2	n/a	n/a	n/a	n/a	n/a	n/a
	G051114#l	15.8	10.5	5250	26.4	45.6	7.6	26.8	2.1	n/a	n/a	n/a	n/a
	G290915#2	18.2	12.1	4890	23.6	32.3	3.5	n/a	n/a	n/a	n/a	n/a	n/a
	G040315#4	20.0	13.3	5050	24.7	54.6	5.8	9.9	0.5	5.3	0.3	0.10	0.01
	G110914#l	50.0	33.3	5260	26.4	52.9	5.1	15.1	2.5	15.1	0.3	0.29	0.03
Type B	G110914#2	5.0	3.3	965	2.5	15.2	0.9	n/a	n/a	9.4	1.9	0.62	0.05
sand	S071114#l	10.0	6.7	802	1.9	19.8	2.5	11.5	1.5	7.8	0.8	0.39	0.06
	G250914#2	15.2	10.1	982	2.5	30.9	1.0	13.4	2.8	8.0	0.5	0.26	0.02
	G240714#l	8.0	5.3	3170	12.3	25.6	1.7	20.3	3.7	n/a	n/a	n/a	n/a
	G300714#2	13.8	9.2	3240	12.7	25.4	6.0	24.9	6.9	n/a	n/a	n/a	n/a
	G070814#l	30.0	20	3070	11.8	43.9	1.7	23.2	3.1	12.5	0.4	0.28	0.02
	G280515#5	4.3	2.9	5350	27.2	27.5	3.8	21.9	1.9	13.9	3.2	0.51	0.07
	G150814#2	8.0	5.3	5080	25.1	28.0	2.7	n/a	n/a	17.8	2.2	0.64	0.06
	G240415#2	8.8	5.9	5250	26.4	27.7	2.1	21.9	4.9	13.4	1.5	0.48	0.04
	G051016#l	11.9	7.9	4940	24.0	40.5	5.3	n/a	n/a	11.3	0.9	0.28	0.03
	G040315#l	16.0	10.7	5000	24.5	32.3	3.0	n/a	n/a	13.9	0.9	0.43	0.04
	G070515#2	27.2	18.1	5280	26.6	62.3	5.8	38.0	9.3	20.2	0.7	0.32	0.04
Type C	G290916#l	0	0	5130	59.6	17.8	1.9	n/a	n/a	4.1	-	0.23	0.04
basalt	G261016#l	7.3	4.9	5060	24.9	40.6	7.3	n/a	n/a	n/a	n/a	n/a	n/a
	G030215#l	10.0	6.7	5200	26.0	54.9	2.4	14.3	0.9	n/a	n/a	n/a	n/a
	G280515#3	12.0	8	5290	26.7	39.0	4.2	16.9	1.9	n/a	n/a	n/a	n/a
	G030215#3	15.0	10	5210	26.1	58.9	2.5	16.5	2.4	n/a	n/a	n/a	n/a
	G130515#2	15.2	10.1	5190	25.9	38.4	2.5	n/a	n/a	n/a	n/a	n/a	n/a
	G280515#2	17.0	11.3	5260	26.5	41.9	4.4	24.4	0.7	n/a	n/a	n/a	n/a
Type D	S311014#l	80	53.3	930	2.3	25.0	1.8	15.7	1.9	8.6	0.1	0.34	0.03
solid ice	S031014#l	80	53.3	977	2.5	30.4	4.0	8.2	1.3	7.5	0.1	0.25	0.04
	G300714#l	80	53.3	3020	11.5	58.7	9.7	17.2	0.6	10.6	0.1	0.18	0.03
	G190914#l	80	53.3	4960	24.2	64.9	12.2	24.0	4.4	16.8	0.2	0.26	0.05

*Calculated using the Planar Impact Approximation (see Melosh 1989). Data for C and S in the linear wave speed equation were taken from Ahrens and Johnson (1994) for Al and basalt, and Senft and from Stewart (2008) for ice.

41.2 ± 10.7 mm for 16.1 mm (10.7) ice thickness. Larger radial fractures were observed within all the targets and usually between five and seven individual fractures. One circular fracture is also observed for the ice thickness >8 mm (5.3).

(b) Nonpenetrative Impacts

At ~1 km s^{-1}, an impact on an ice layer thickness of 15 mm (10.1) produced a nonpenetrative, bowl-shaped crater with a mean diameter and depth of 30.9 ± 1.0 mm and 8.3 mm, respectively. This crater produced a noncircular rim to the crater with seven fractures extending away from the point of impact. No circular fractures were observed as a result of this impact (Fig. 4a).

At ~3 km s^{-1}, the impact in the 30 mm (20) thick ice crust target produced a bowl-shaped crater in the ice with a mean diameter of 44.0 ± 1.7 mm and a depth of 11.5 mm. The crater and the surrounding area were crushed forming a white region around the crater. Seven radial fractures were observed extending away perpendicular in all directions from the point of impact. However, around the crater rim, there remained a network of numerous small fractures producing a discolored white region directly around the crater rim.

At an impact speed of 5 km s^{-1}, a nonpenetrative impact occurred only in an ice thickness of 27.2 mm (18.1), producing a barely recognizable crater within a completely disrupted ice layer (Fig. 4b). The ice layer became completely fractured with larger centimeter-sized blocks of ice forming as the fractures propagated through the ice. The impact crater was only recognizable from the crushed ice that surrounded the point of impact similar to the features observed in other impacts onto ice target. At the point of impact, the ice had been crushed to a very thin sheet of 1–2 mm thick.

Ice Over Basalt

The shots at type C targets had a mean impact speed of 5.19 ± 0.08 km s^{-1}. The craters produced in the target with 10 mm (6.7) to 17 mm (11.3) ice crust thickness (Figs. 5a and 5b) were formed within the ice layer only and did not penetrate into the denser basalt material below the ice. Indeed, the basalt appeared to form an immovable barrier into which the ice was crushed at the point of impact, forming a hole in the ice with a crushed ice center above the unaltered basalt material creating a raised feature within the crater at the point of impact. In two cases, the ice was removed from the region immediately around this central crushed ice area as spall, exposing the basalt below. The resulting overall holes/craters in the ice were shallow and wide, with an average diameter of 54.9 ± 2.4 mm and 58.9 ± 2.5 mm for the 10 mm (6.7) ice thickness and 15 mm (10) ice thickness, respectively. However, this degree of spallation was not observed in other type C targets with similar ice thicknesses of 12 mm (8), 15.2 mm (10.1), and 17 mm (11.3), which produced small craters with mean spall diameters of 39.0 ± 4.2, 38.4 ± 2.5, and 41.9 ± 4.4, respectively (Fig. 5b). Due to the variation of the degree of spallation of the ice crust, the data for type C targets fall into two groups based upon the mean crater diameter; group 1 experience high level of spallation producing larger craters, and group 2 experience lower level of spallation producing mean cater diameters more akin to that produced in the other target types A and B < 50 mm (33.3) (Table 1).

Radial fractures travelled through the surviving ice crust and extended away to the edges of the target, causing disruption of the ice crust far beyond the edge of the crater. Partial and full circular fractures are observed away from the point of impact. These circular fractures are similar to those observed in soda lime glass targets, which Burchell and Grey (2001) assigned them to edge effects on finite targets. However, similar features are also reported in brittle targets of silica plates (Michel et al. 2006). In this latter case, Michel et al. assigned the features to internal cracking linked to attempted spallation.

One of the issues with this target type is the small area of basalt and the large region of sand below the ice layer. Therefore, an additional shot was undertaken at 5.06 km s^{-1} (G261016#1), with a larger basalt target (100 × 200 mm) with an ice thickness of 7.3 mm (4.9). Similar to the previous results, the ice was removed as spall with no impact damage on the surface of the subsurface basalt layer. The ice did not produce an area of crushed ice in the center of the impact but produced a spall region of 40.6 ± 7.3 mm. The large standard deviation is due to the elliptical nature of the crater formed. No circular fractures were produced but seven radial fractures extended a similar angle around and away from the point of impact to the edge of the target. The hole produced in this ice layer is similar in diameter with those produced in the other impact in type C results; this indicates that the diameter in the other shots was not significantly influenced by the smaller basalt targets used originally.

We also conducted an impact onto the basalt target without the ice crust, with the 1.5 mm Al projectile fired at 5.13 km s^{-1} (G290916#1). This produced a small, bowl-shaped crater on the basalt surface, of diameter 17.7 ± 1.9 mm, with no fractures observed on surrounding the surface. This demonstrated that the unimpeded input of the projectile directly onto the basalt

at these speeds does indeed produce a crater in the basalt. The absence of such a crater in the other type C shots is therefore due to the presence of the ice layer.

Solid Ice

An 80 mm (53.3) deep ice target was used as a standard for all the impact speeds studied with solid ice (type D) targets. The impacts on these targets produced clear bowl-shaped craters at all impact speeds (Fig. 6). After impact, the ice surfaces also included numerous small radial fractures that extended away from the point of impact, often forming numerous terraces where the surface ice was lost during the impact. In addition to radial fractures, at a shot speed of 5 km s^{-1}, circular fractures were observed up to 50 mm away from the point of impact, and some circular structures around the crater were observed at impact speed of 3 km s^{-1}. These fractures encompass the whole crater and connect the radial fractures together. The circular fractures can be clearly observed (Fig. 6); however, they sometimes lay within the ice without reaching the surface and are similar to those observed in the type C targets which resemble the concentric fractures reported in impacts into glass and other brittle materials (Burchell and Grey 2001; Michel et al. 2006).

At the lowest speed of 0.9–1 km s^{-1}, both impacts produced craters, which were bowl-shaped in their outer regions with mean diameters of 25.0 ± 1.8 mm and 30.4 ± 7.5 mm, and depths of 8.6 mm and 7.5 mm with a central pit in each crater. This is the classic crater shape observed in thick brittle targets such as ice (e.g., Fendyke et al. 2013) or glass (e.g., Burchell and Grey 2001). An interesting feature is the regularity of the radial fractures. Six radial fractures were produced (in shot S031013#1) extending up to 100 mm away from the crater at almost equidistant angles. The fractures extended downward from the surface creating planar features within the ice (Fig. 6a). At this lowest speed, no circular fractures or cracks were produced, indicating that the production of the circular fractures is a function of the speed of the impact.

At 3 km s^{-1}, the crater formed was similar in shape to those produced by an impact at ~1 km s^{-1}, but larger in diameter (58.7 ± 9.7 mm) and depth (10.6 mm). However, both these did not grow in the same proportion compared to the lower speed shot, producing a lower depth/diameter ratio of 0.18 (see Table 1).

At the impact speed of 5 km s^{-1}, the impact crater (diameter 64 ± 12 mm, depth 16.8 ± 0.2 mm) was only slightly larger than those observed with the 20 mm (13.3) and 50 mm (33.3) thick ice layers over water, and a 27 mm (18.1) thick ice layer over sand impacts (see Table 1). This suggests that in the latter cases, the targets were effectively acting as almost semi-infinite ice targets. We can also compare to previous work for 1.5 mm aluminum projectiles impacting solid ice at 5 km s^{-1}. Burchell and Johnson (2005) reported an impact in solid ice by a 1.5 mm Al projectile at 4.87 km s^{-1} (very similar to the impact speed here of 4.96 km s^{-1}). They found a crater diameter of 89 ± 8 mm and a depth of 13.3 ± 0.1 mm. However, the impact in Burchell and Johnson (2005) was at normal incidence, whereas here it was at 45°. In a separate paper concerning impacts on ice targets, Grey et al. (2002) found that around 45° incidence is when crater diameter starts to decrease due to the nonnormal incidence. The crater depth, however, decreases immediately when an impact is at nonnormal incidence (with a decrease of 10% at 45°). This suggests that the crater seen here in solid ice at 45° incidence is slightly narrower and deeper than expected.

DISCUSSION

We have explored the influence of the ice layer thickness on the resulting crater morphology of an impact in a variety of impact scenarios described in the results section. The results are discussed in more detail below.

Variation in Crater Morphology With Ice Thickness at 5 km s^{-1}

Figure 7 shows the mean spall diameter of a crater versus the thickness of the ice for impacts at 5 km s^{-1}. In the cases of ice over water and ice over sand (target types a and b), there is a strong growth in crater spall diameter as the ice thickness increases to 20–27 mm (i.e., a normalized ice thickness of some 13–18 times the projectile thickness). At the normalized (ice thickness/projectile diameter) value of 33.3 in ice over water (G110914#1) and 18.1 in ice over sand (G070515#2), the crater diameter is similar to that in the semi-infinite ice target at 5 km s^{-1} (G190914#1), i.e., around (52 ± 5.1)–(65 ± 12.2) mm.

To fit these trends, it is assumed that the crater diameter no longer increases in the thicker ice targets. So ice thicknesses above 30 mm (15 × projectile diameter) were excluded. A linear fit of crater diameter (d) versus ice thickness (D) or ice thickness normalized to projectile diameter (N) was made to the remaining data (more complicated or higher order functions do not in general improve the fits). The data were fit separately for each target type.

For ice over water, this yielded (solid lines in Fig. 7):

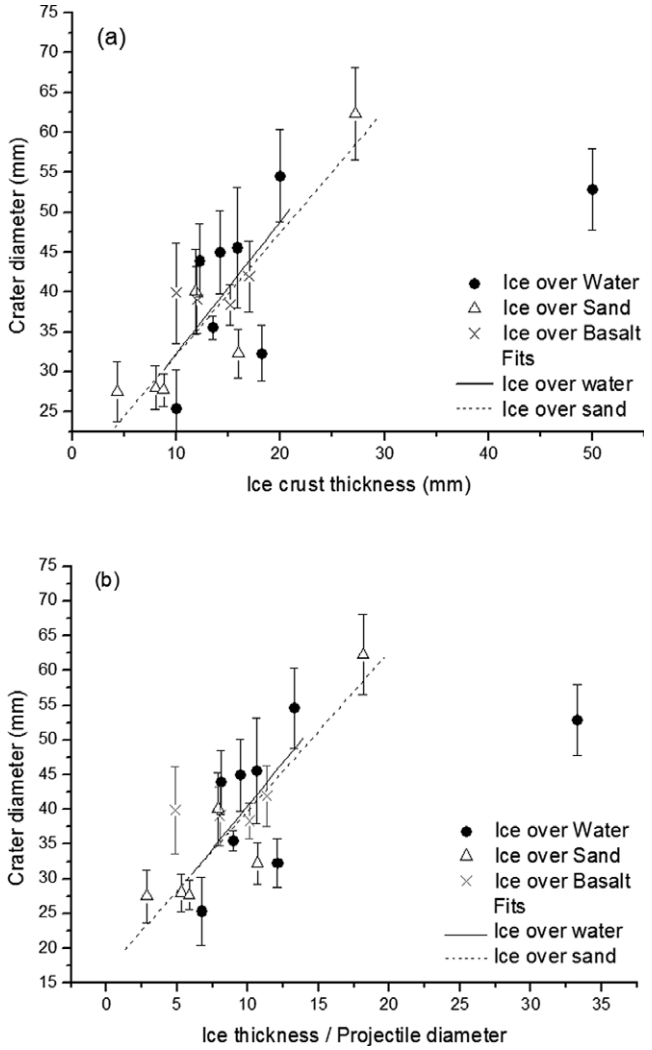

Fig. 7. Relationship between ice crust thickness and mean diameter of crater for all three target types for impacts at 5 km s^{-1}. a) Crater diameter versus absolute ice thickness. b) Crater diameter versus ice thickness normalized to projectile diameter. Gray cross—ice over basalt; black circles—ice over water; and triangle—ice over sand. Error bars show 1 σ standard deviation of the mean value. The fit curves are described in the main text and are labeled by the name of the data set they apply to. The solid lines are the fits for ice over water (Equations 1 and 2) and the dashed lines ice over sand (Equations 3 and 4).

$$d = (6.3 \pm 12.0) + (2.6 \pm 0.8)D, \quad r^2 = 0.67, \quad (1)$$

$$d = (6.2 \pm 12.4) + (3.9 \pm 1.3)N, \quad r^2 = 0.67. \quad (2)$$

For ice over sand, the results were (dashed lines in Fig. 7):

$$d = (17.2 \pm 4.2) + (1.3 \pm 0.4)D, \quad r^2 = 0.70, \quad (3)$$

$$d = (17.1 \pm 4.2) + (1.9 \pm 0.5)N, \quad r^2 = 0.70. \quad (4)$$

In all cases, the r^2 value (square of the regression coefficient), which is used as goodness of fit, is reasonable.

It is less clear what is happening for ice over basalt (type C targets), where the scatter on the data combined with the narrow range of ice thicknesses obscure any trend.

Often in impact cratering studies, the ratio between the crater depth (H) and the crater diameter (D) is used to consider overall crater morphology. Here, however, there are three general cases of craters (1) where the crater failed to penetrate the ice, (2) where the ice was penetrated but no further cratering occurred in the subsurface layer, and (3) where cratering continued in the subsurface region. Furthermore, to add more complexity to the data here, in the case of ice over water targets, the depth of crater formation in the subsurface water was not determined.

Taking case (1) first. The H/D versus ice thickness data for nonpenetrative impacts at 5 km s^{-1} are shown in Fig. 8. The pure ice target impacted at 5 km s^{-1} had $H/D = 0.26 \pm 0.05$. Given the typical scatter on the data, this is compatible with previous measurements of this ratio (e.g., see Shrine et al. [2002] who found $H/D = 0.23$ at 5 km s^{-1}). The ice over water data had two nonpenetrative impacts with $H/D = 0.10 \pm 0.01$ and 0.29 ± 0.03. It is the higher of these, which corresponded to thicker ice (normalized diameter = 33.3), which is compatible with the semi-infinite ice case (Fig. 8). In the case where ice thickness was 13.3 × projectile diameter, there was no penetration but the resulting crater sides were shallower than expected.

For case (2), i.e., where the ice is penetrated but there is no evidence of cratering in the subsurface, the ratio crater depth/diameter is given by the ice thickness/crater diameter. For impacts on ice over basalt targets, this ranges from 0.18 to 0.53, increasing with increasing ice thickness.

The case (3) events (at 5 km s^{-1}), i.e., which penetrate the ice and cause subsurface damage, have craters with H/D ratios >0.28 (0.28 to 0.64), and the thinner the layer, the larger the H/D value. For the thinnest ice, some 5–11 times the projectile thickness, the H/D value was double that found in semi-infinite ice. Thus, the thinner the ice, the relatively deeper the crater becomes. To illustrate this change, in Fig. 8b, we add the data for penetrating impacts in ice over sand to those for the nonpenetrating impacts already shown in Fig. 8a.

The ice over sand and ice over water data in Fig. 8 show three groups which correspond to three regions,

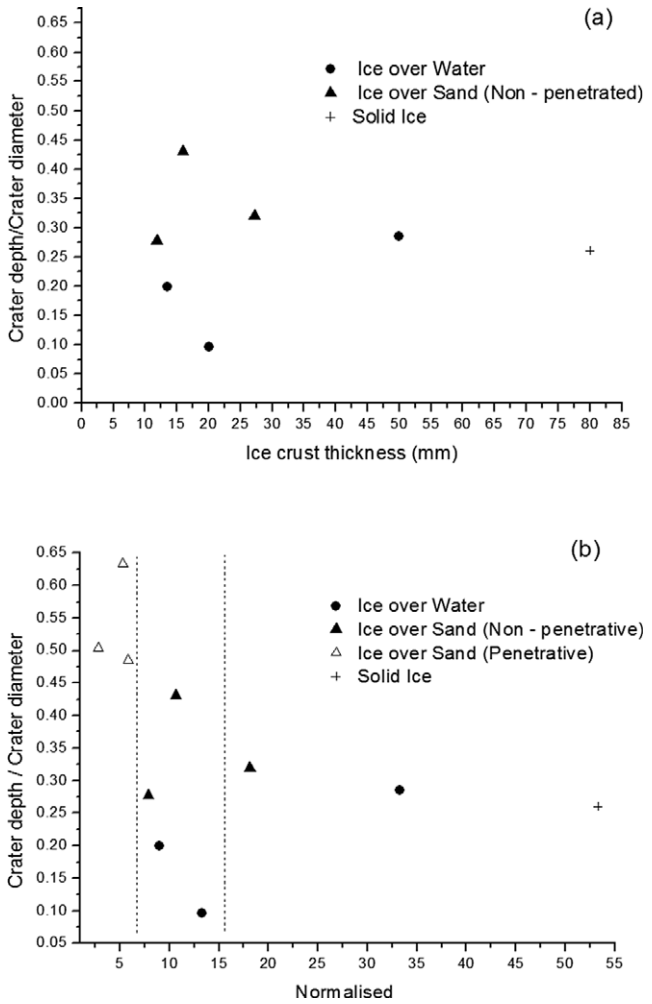

Fig. 8. a) The ratio of crater depth/diameter versus absolute ice crust thickness for nonpenetrating impacts at 5 km s^{-1}. b) The same data as (a) with the addition of three penetrating impacts in ice over sand, and the data are plotted versus ice thickness normalized to projectile diameter. The vertical dotted lines in (b) show the values that divide the penetrative, transitional, and semi-infinite regions (see text).

penetrative, transitional, and semi-infinite, which result in different crater morphologies. Penetrative impacts occur when the ice is about <7 times the projectile thickness. The value of 7 is taken as the midpoint between data points which seem to lie in the respective neighboring regions. These data points are at 6 and 8, respectively, giving a boundary of 7 with an uncertainty of ±1. The transition region occurs at ice thicknesses between 7 and 15.5 times the projectile diameter; these craters do not penetrate the ice layer and this zone is discussed further below. The upper boundary of this region lies between data points at approximately 13 and 18 times the projectile thickness. The boundary is thus taken as 15.5 ± 2.5. When greater than 15.5 times the projectile diameter, the ice has such a substantial thickness that the layer acts as a semi-infinite target. The substrate below then has no bearing on the crater produced. These boundaries are summarized in Table 2. From Fig. 8, we can also see that the critical value of crater depth/diameter between penetrating and nonpenetrating impacts is approximately 0.45.

Impacts in the transitional zone will usually result in nonpenetrative impacts, but the craters have significantly smaller diameters than the craters that form in the semi-infinite zone. Figure 9 shows the variation of the craters through all three regions and the relationship between the depth/ice thickness ratio (H/I_t) and the resulting crater diameter. In Fig. 9, the data above a H/I_t value of 1 are penetrative impacts, with the nonpenetrative impacts falling below 1. The ice over sand data exhibit an exponential-like behavior, with the transitional region sitting at the point of inflection of the curve. Within the transitional region, it is clear that the two ice over sand impacts have a H/I_t ratio of 0.9, showing how close to the boundary of penetrative and nonpenetrative impacts these data points sit. In this transitional region, it is the impedance and porosity of the subsurface material which likely plays a substantial role in the formation of the various crater morphologies. At this point, pore collapse may occur in the subsurface sand layer, producing a deeper crater than expected in the ice. The ice over water data show the beginnings of a similar trend; however, due to the different impedance of the subsurface water, the transitional curve falls below that of the ice over sand data points.

An indicative fit is shown to the data in Fig. 9 as a solid curve. The fit is of the form y = a + b * exp(−kx), where y is crater depth/ice thickness, and x is crater diameter. We find:

$$y = 0.44 + 8.6 \times 10^{6} e^{-0.55x}, \quad r^2 = 0.81. \tag{5}$$

Although r^2 is fairly high, the fit itself is unstable. It is very sensitive to the convergence criteria used and the particular data points included in the fit. Given that we suppose that the path through the transition region depends on the properties of the subsurface layer, this is perhaps not a surprise. For this reason, we suggest that the fit in Equation 5 be taken as indicative of expected behavior, rather than definitive.

For fully penetrating impacts, just as for those in semi-infinite ice, the presence of the ice layer becomes less significant as its thickness decreases (or increases in the case of the infinite ice). The data for the various target types are thus expected to converge to a common trend.

Table 2. Generic crater shape dependent on ice thickness and subsurface layer composition. H/D is crater depth over diameter. The boundary at 7 times the projectile thickness is uncertain at ±1, while that at 15.5 is uncertain at ±2.5.

Ice thickness/ projectile diameter	Subsurface layer characteristics	Crater shape
<7	Low strength	Penetrative region Narrow, relatively deep, H/D increasing to 0.65 in the thinner ice layers
	Dense, high strength	Wide craters with flat floors, steep ice walls, and possible central peak of heavily fractured and compressed ice. H/D from 0.5 to 0.2
7–15.5	N/A	Transitional region Becoming deeper and narrower, H/D falls from 0.45 to 0.1 Impedance of subsurface layer may play a significant role
>15.5	N/A	Semi-infinite region Shallow bowl shaped crater in ice, H/D = 0.275

VARIATION IN CRATER MORPHOLOGY WITH SUBSURFACE MATERIAL DENSITY

Besides overall shape, given by crater depth and diameter, it is also possible to characterize craters by the variation in shape along a cross-sectional profile taken across a crater. Three distinct crater profiles have been observed during this study (Fig. 10). These appear correlated with the subsurface medium beneath the ice. The first type occurs for impacts into a homogenous material, i.e., the nonpenetrative impacts that occur in the ice crust alone. These produced relatively shallow profiles, with wider outer areas arising from the production of spall (Fig. 10a). The second profiles are produced by craters that form when entering a second medium with a lower porosity than that of the first layer. This was observed in the ice over saturated sand targets (Fig. 10b), and resulted in a deepening of the crater. The final profile was produced when the second medium had a greater density and strength than the first (Fig. 10c). In the case of having a basaltic subsurface, the energy of the projectile was not sufficient to penetrate or even visibly damage the subsurface resulting in a shallow crater with an elevated pitted central region. In such craters, the outer walls of the "hole" in the ice layer were very steep.

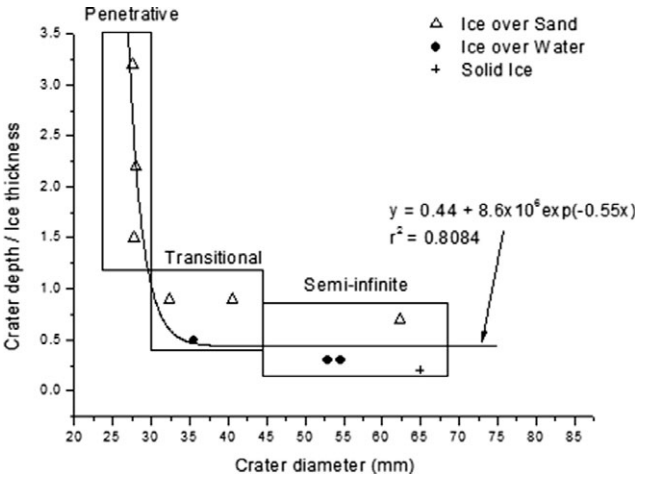

Fig. 9. The ratio of crater depth/ice thickness versus the crater diameter, for impacts at 5 km s^{-1}. The boxes represent the three zones identified in the text highlighting the change from penetrative to transition, and the semi-infinite regimes. For the ice over water data, only those impacts which produced nonpenetrative craters are shown. The solid curve is a fit to the data and is further described in the main text (Equation 5).

Such a variation in crater morphology based on the density variation of multiple layers in the target observed here agrees with the results from Arakawa et al. (2000, 2002), who used stratified targets produced by heating from the top-down. Arakawa et al. (2000) looked at craters forming within a body with a more porous interior than surface. This influenced overall crater growth so much that it could even result in major excavation of the less dense material in the interior of the target to a greater lateral extent than the visible crater in the surface. Arakawa et al. (2002) found that a crater forming in a body with a lower density surface material above a higher density interior material could result in the crater formation ceasing abruptly at the boundary between the layers, forming a flat bottom to the crater at the horizon of the denser layer.

Thus, in general, flat bottom craters which appear to be shallower than expected show that the impact occurred in a layered material, with the upper layer having less strength than the lower layer. This is well observed for example on the Moon (see Wilcox et al. [2005] or Bart [2014]) and reproduced in laboratory studies of impacts on sand over basalt (e.g., Burchell et al. 2015). However, where the impact has occurred in a layered target, where it is the top layer that is the strongest and most cohesive, the influence of the subsurface on the overall crater shape needs to be inferred by considering the steepness of crater walls in cross-sectional profiles. This set of conditions is summarized in Table 2.

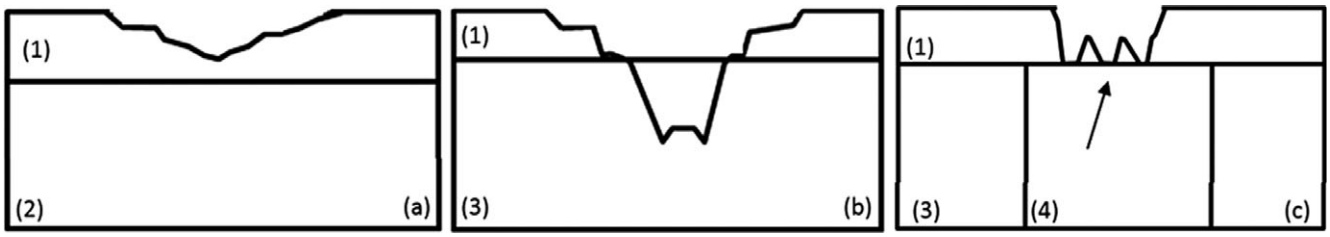

Fig. 10. Schematic of the crater produced within a multilayered target impacted at 5 km s^{-1}. a) Crater formed in homogenous ice layer. b) Crater formed in target of ice over sand (greater porosity). c) Crater formed in ice over basalt (greater density) and which shows the central feature of crushed ice on the floor of the crater with the pitted region showing the point of impact (black arrow). Material types are labeled as: (1) Clear ice, (2) Water, (3) Saturated sand, and (4) Basalt.

Variation in Crater Morphology With Impact Speed

The impacts onto solid ice and onto ice over sand were repeated at a range of lower impact speeds (1 and 3 km s^{-1}), as well as the 5 km s^{-1} discussed so far—see Table 1. We divide the ice over sand data into three ice thickness regimes: 5–9 mm, 10–20 mm, and >20 mm. In each case, crater size increases with the increasing impact speed (Fig. 11). Shrine et al. (2002) reported that crater diameter in semi-infinite ice depends on impact speed (in km s^{-1}) to the power 0.72. We show such a curve as a solid line on Fig. 11, normalized to the crater size at 1 km s^{-1}. The solid curve fairly well describes the data here for impacts in thick and semi-infinite ice. However, a power of 0.72 does not describe the craters in thinner ice. For the case of ice thickness <10 mm, we found a power of 0.37 was more appropriate. This suggests that crater diameter in thin ice surfaces is significantly less dependent on impact speed than for semi-infinite ice, and that the relatively thinner the ice layer (compared to projectile size), the less the dependence.

COMPARISON WITH OBSERVED CRATERS ON MARS AND EUROPA

Mars

The craters produced in this study can be compared to the ice over basalt data simulations in the work by Senft and Stewart (2008). The impact speed used in their calculations was 10 km s^{-1}, which is close to the median impact velocity of asteroids impacting Mars of 12.8 km s^{-1} (Bottke et al. 1994) and twice the maximum impact speed in our experiments here. Senft and Stewart (2008) modeled, among other configurations, impacts of a projectile onto a surface ice layer over subsurface basalt, similar to one of the configurations in the laboratory experiments reported here. They found that the presence of an ice layer significantly modified the cratering mechanics and resulted in a range of observable effects on the final crater morphology. In the simulations, the presence of an ice layer above the basalt basement resulted in a bowl-shaped crater in the subsurface basalt, a result not observed here. However, not only was the impact speed greater in Senft and Stewart (2008) than that here but also they used a maximum ice thickness only twice that of the projectile diameter, by contrast the experiments here were at lower speeds and had the ice layer over basalt at least six times greater than the projectile thickness.

The distinctive craters observed here in the ice over basalt targets, produced a crater with a raised but pitted central feature within a broader flat floor crater leading to the crater edge (Fig. 5). At the point of impact lies a mound of crushed ice with a depression at the tip. If such a feature was viewed from orbit, such a mound could be interpreted as a central peak (it should be noted that such central peaks would not be the classical central peak that appear in large rocky craters). Such features have been observed on Mars, Callisto, and Ganymede (Schenk 1993; Barlow 2010), and have been described as central pits in craters. Central pits are described as circular to elliptical depressions in the center of many Martian impact craters, either directly on the crater floor or atop a central rise or peak. Previous models for the formation of such peaks include vaporization of the subsurface volatiles and explosive release of the subsequent gases (Wood et al. 1978), collapse of target materials (Greeley et al. 1982), or excavation into a subsurface liquid layer (Croft 1983).

Interestingly, the observation of such impact craters on Callisto and Ganymede may provide information about the interiors of these bodies. These craters only formed on targets with much denser material below the ice crust, which leads to the suggestion that at the point at which central pits are observed in crater on these icy moons, there is no subsurface ocean but instead a direct contact between the ice crust and a denser, possibly basaltic, material. Alternatively, if there was penetration into a pressurized subsurface ocean, an upwelling of liquid material might occur in the center, which then freezes as a central peak. Note that this type of physical set-up was not reproduced in the experiment set-up here, so is untested in the current work.

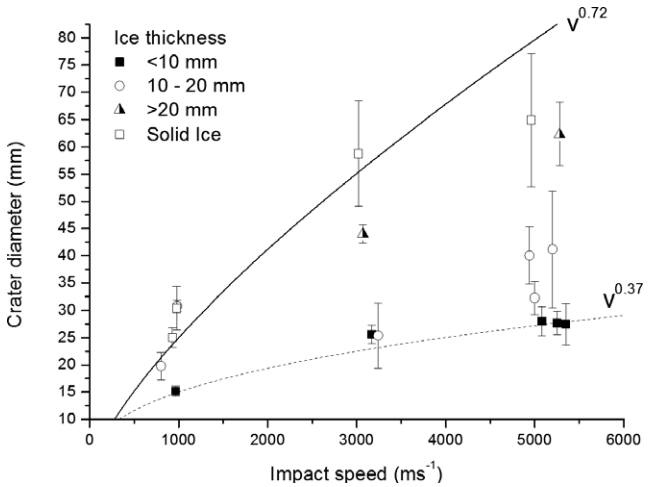

Fig. 11. Relationship between the impact speed and the crater diameter formed within the ice crust above a sand subsurface, with the data divided into three ranges of ice thickness. For comparison, data for impacts in solid (effectively semi-infinite) ice targets are also shown. Error bars show 1 σ standard deviation of the mean value. The curve shown as a solid line is a power law where crater diameter in semi-infinite ice depends on impact speed (in km s^{-1}) to the power 0.72 as suggested by Shrine et al. (2002). For the very thin ice (<10 mm thickness), we show a dashed curve where the power law is 0.37.

Europa

Impact craters on Europa have been previously classified into two groups by Lucchitta and Soderblom (1982) (1) impact features including craters Govannan and Pwyll that have much in common with the classic impact craters observed on the Moon and other dry silicate bodies and (2) features which lack obvious continuous rims or central peaks and which are very flat at the scale of the whole feature. These latter crater types, such as Callanish and Tyre, owe their identification as impact features mostly to fields of secondary craters radially spread about them.

The faulting/rays associated with the Pwyll crater (Fig. 1) show a similar configuration to those formed in the experiments here, with a multitude of small fractures around the crater and longer established faults extending away from the point of impact. Pwyll crater, however, appears to have no associated circular fractures which are observed as features of the Callanish and Tyre craters.

It is believed that the Callanish and Tyre craters are formed in ice above a subsurface ocean (Moore et al. 2001); they are dominated by the lack of surface features including crater rims, central peaks, and crater rim relief. These are similar to the penetrative impacts produced in this study. The penetrative impacts produced round bullet-like holes that did have steep crater edges; however, over time after the impact, the ocean below the surface would refreeze and much of the crater edge would become lost. These craters are described as being narrow and deep. Circular features are also observed in these impact types similar to the terrace circular features observed around the Callanish crater.

In general, the results in the laboratory here are similar to those described by Bray et al. (2014), who reported on simulations of impacts into ice over water with regard to impacts on Europa. Bray et al. (2014) suggested that full penetration of the (Europan) ice shell occurs when the ice thickness is less than ~7 times the projectile diameter. However, it should be noted that these simulations used kilometer-scale thicknesses and an impact speed of 15 km s^{-1}.

The hydrocode modeling of Cox and Bauer (2015) also investigated the requirements for a breaching impact of Europa's ice, and the interaction between the crust and the subsurface material. They again performed calculations at 15 km s^{-1} impact speed, but then scaled their results to 26.5 km s^{-1}, the mean impact speed for Europa (Zahnle et al. 2003). Cox and Bauer (2015) reported a correlation between the crater size and the thickness of the ice crust, with the thinner ice producing cavities of the transient crater that are deeper relative to their width than the crater produced in the deeper ice crusts. They also found that the transition between penetrating and nonpenetrating impacts on Europa involved ratios of transient crater depth/diameter around 0.45 (Fig. 2, Cox and Bauer 2015). This is similar to what we found here in Fig. 8, where transition between penetrating and nonpenetrating impacts occurs at around depth/diameter = 0.45. Interestingly, despite the difference in speed and size scales, this transition in the modeling of Cox and Bauer (2015) occurred for ice thicknesses some 9–11 times the projectile diameter (for ice thickness between 8 and 13 km, respectively), not too dissimilar to the boundary observed here of 15.5 ± 2.5 times the projectile thickness despite the dissimilar scales and speeds. We also note that Cox and Bauer found that the transient cavity in a crater only had to exceed 90% of the depth of the ice layer of the layer to be effectively breeched, again similar to that observed here (Fig. 9).

Here we do not attempt a full scaling to solar system scales. However, we note that one of the key variables often used in such work is:

$$\pi_r = r\left(\frac{\rho_p}{m}\right)^{1/3}, \tag{6}$$

where r is radius of the crater, and m and ρ_p are the mass and density of the projectile (Holsapple and Schmidt 1982).

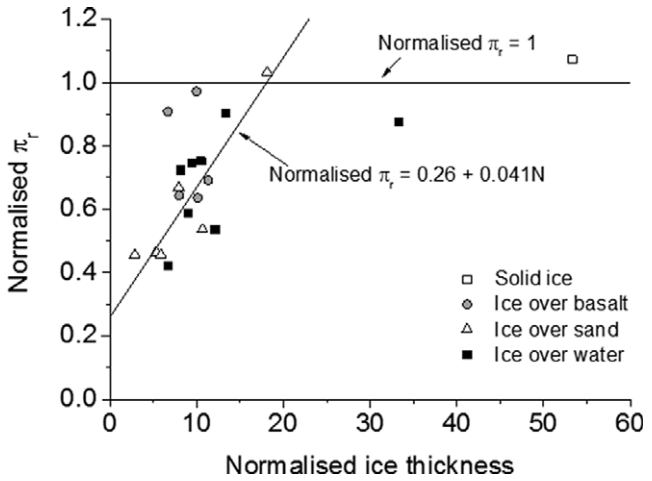

Fig. 12. Data for π_r versus normalized ice thickness for impacts at ~5 km s^{-1}. The π_r data have been normalized to its mean value at large ice thicknesses. The solid lines show a linear rise in π_r at low ice thickness (slope of 0.041), reaching a maximum of 1 above normalized ice thickness greater than 15.5.

In Fig. 12, the data are shown for π_r (normalized to 1 at large ice thicknesses) versus normalized ice thickness (N). For normalized ice thicknesses <15.5, the π_r values fall as normalized ice thickness falls. For ice over sand we found:

$$\text{normalized } \pi_r = 0.28 + 0.038N, \quad (7)$$

and for ice over water we found:

$$\text{normalized } \pi_r = 0.26 + 0.041N. \quad (8)$$

In both cases, the results are similar and we show the curve for ice over water on Fig. 12. The data for ice over basalt gave no good fit, and two of the data points lie noticeably above the fits for ice over water and sand, suggesting a possibly steeper dependence of the slope and that the transition point is at a slightly lower normalized ice thickness. This is commensurate with a different path through the transition zone for ice over basalt. These results nevertheless suggest it is in general possible to predict the change in crater diameter in a thin ice surface over a different substrate. The implication at the scale of the experiments here is that there is a 4% increase in crater diameter as an extra projectile's thickness of ice is added to the icy surface.

CONCLUSIONS

This work investigates the influence on impact crater morphology of the thickness of ice crusts over different substrates. Several types of layered target were considered, with a subsurface layer of sand, basalt, or liquid water. Each type influenced crater morphology differently, suggesting that the crater shape is dependent on the subsurface material when the ice layer is less than 15.5 ± 2.5 times the projectile diameter (see Table 2 for a summary). At the highest speeds here (5 km s^{-1}), penetration of the surface layer occurred when the ice layer was less than some 7 ± 1 times the projectile diameter. In the case of a basalt subsurface layer, no damage was observed to the exposed basalt in the experiments where the ice layer was breached. However, it should be noted that the ice layer in such cases was still at least six times the projectile thickness.

The crater diameter is also sensitive to the thickness of the surface ice layer. For effective semi-infinite ice thickness (>15.5 times the projectile thickness), there is no influence. However, as the ice thickness is reduced below this, we find a 4% reduction in crater diameter for each reduction of one projectile thickness worth of ice. We also found that the diameter of the crater in the surface ice layer scaled with impact speed to the power 0.72 for thick ice layers over sand, as suggested for semi-infinite ice by previous work (Shrine et al. 2002). However, this dependence decreased as ice thickness decreased, being smallest in the thinnest ice.

This pattern of results indicates that the crater shape is dependent on a combination of impact speed, ice layer thickness, and the nature of the subsurface material. There is also information about the target material contained not just in the overall size and shape (depth/diameter) of the craters, but also in shape profile across a crater, the degree of damage to the surrounding ice, and even the steepness of the walls in the ice at the edge of the craters.

Acknowledgments—The authors thank Mike Cole for his aid with the light-gas gun at the University of Kent. The impact work was funded by the Science and Technology Faculty Council (UK). The authors thank the reviewers and editor for detailed comments which helped improve this manuscript.

Editorial Handling—Dr. Michael Poelchau

REFERENCES

Ahrens T. J. and Johnson M. L. 1994. *Shock wave data for minerals*. In *Mineral physics and crystallography: A handbook of physical constants*, edited by Ahrens T. J. Washington, D.C.: American Geophysical Union. pp. 143–184.

Arakawa M. 1999. Collisional disruption of ice by high-velocity impact. *Icarus* 142:34–45.

Arakawa M., Higa M., Leliwa-Kopystyński J., and Maeno N. 2000. Impact cratering of granular mixture targets made of

H 2 O ice–CO 2 ice–pyrophylite. *Planetary and Space Science* 48:1437–1446.
Arakawa M., Leliwa-Kopystynski J., and Maeno N. 2002. Impact experiments on porous icy-silicate cylindrical blocks and the implication for disruption and accumulation of small icy bodies. *Icarus* 158:516–531.
Barlow N. G. 2010. Central pit craters: Observations from Mars and Ganymede and implications for formation models. *Geological Society of America Special Papers* 465:15–27.
Barlow N. G. 2015. Constraining geologic properties and processes through the use of impact craters. *Geomorphology* 240:18–33.
Bart G. D. 2014. The quantitative relationship between small impact crater morphology and regolith depth. *Icarus* 235:130–135.
Bottke W. F., Nolan M. C., Greenberg R., and Kolvoord R. A. 1994. Velocity distributions among colliding asteroids. *Icarus* 107:255–268.
Bray V. J., Collins G. S., Morgan J. V., Melosh H. J., and Schenk P. M. 2014. Hydrocode simulation of Ganymede and Europa cratering trends—How thick is Europa's crust? *Icarus* 231:394–406.
Burchell M. J. and Grey I. D. S. 2001. Oblique hypervelocity impacts on thick glass targets. *Materials Science Engineering A* 303:134–141.
Burchell M. J. and Johnson E. 2005. Impact craters on small icy bodies, i.e. icy satellites and comet nucleus. *Monthly Notices of the Royal Astronomical Society* 360:769–781.
Burchell M. J., Brooke-Thomas W., Leliwa-Kopystynski J., and Zarnecki J. C. 1998. Hypervelocity impact experiments on solid CO2 targets. *Icarus* 131:210–222.
Burchell M. J., Cole M. J., McDonnell J. A. M., and Zarnecki J. C. 1999. Hypervelocity impact studies using the 2 MV Van de Graaff accelerator and two-stage light gas gun of the University of Kent at Canterbury. *Measurement Science and Technology* 10:41–50.
Burchell M. J., Grey I. D., and Shrine N. R. 2001. Laboratory investigations of hypervelocity impact cratering in ice. *Advances in Space Research* 28:1521–1526.
Burchell M. J., Leliwa-Kopystynski J., and Arakawa M. 2005. Cratering of icy targets by different impactors: Laboratory experiments and implications for cratering in the solar system. *Icarus* 179:274–288.
Burchell M. J., Cole M. J., Ramkissoon N. K., Wozniakiewicz P. J., Price M. C., and Foing B. 2015. SMART-1 end of life shallow regolith impact simulations. *Meteoritics & Planetary Science* 50:1436–1448.
Carr M. H., Belton M. J., Chapman C. R., Davies M. E., Geissler P., Greenberg R., and Veverka J. 1998. Evidence for a subsurface ocean on Europa. *Nature* 391:363–365.
Cassen P. M., Reynolds R. T., and Reynolds R. T. 1982. Structure and thermal evolution of the Galilean satellites. In *Satellites of Jupiter*, vol. 1, edited by Morrison D. and Matthews M. S. Tucson, Arizona: The University of Arizona Press. pp. 93–128.
Chabot N. L., Ernst C. M., Denevi B. W., Harmon J. K., Murchie S. L., Blewett D. T., and Zhong E. D. 2012. Areas of permanent shadow in Mercury's south polar region ascertained by MESSENGER orbital imaging. *Geophysical Research Letters* 39:L09204 https://doi.org/10.1029/2012GL051526.
Clifford S. M., Lasue J., Heggey E., Boisson J., McGovern P., and Max M. D. 2010. Depth of the Martian cryosphere: Revised estimates and implications for the existence and detection of subpermafrost groundwater. *Journal of Geophysical Research* 115:E07001.
Collins G. S. and Wünnemann K. 2005. How big was the Chesapeake Bay impact? Insight from numerical modeling *Geology* 33:925–928.
Collins G. S., Kenkmann T., Osinski G. R., and Wünnemann K. 2008. Mid-sized complex crater formation in mixed crystalline-sedimentary targets: Insight from modeling and observation. *Meteoritics & Planetary Science* 43:1955–1977.
Cox R. and Bauer A. W. 2015. Impact breaching of Europa's ice: Constraints from numerical modeling. *Journal of Geophysical Research: Planets* 120:1708–1719.
Cox R., Ong L. C., Arakawa M., and Scheider K. C. 2008. Impact penetration of Europa's ice crust as a mechanism for formation of chaos terrain. *Meteoritics & Planetary Science* 43:2027–2048.
Croft S. K. 1981. Hypervelocity impact craters in icy media (abstract). 12th Lunar and Planetary Science Conference. pp. 190–192.
Croft S. K. 1983. A proposed origin for palimpsests and anomalous pit craters on Ganymede and Callisto. *Journal of Geophysical Research: Solid Earth* 88:B71–B89.
Fendyke S. F., Price M. C., and Burchell M. J. 2013. Hydrocode modelling of hypervelocity impacts on ice. *Advances in Space Research* 52:705–714.
Giacomuzzo C., Ferri F., Bettella A., Pavarin D., Francesconi A., Flamini E., and Angrilli F. 2007. Hypervelocity experiments of impact cratering and catastrophic disruption of targets representative of minor bodies of the solar system. *Advances in Space Research* 40:244–251.
Greeley R., Fink J. H., Gault D. E., and Guest J. E. 1982. Experimental simulation of impact cratering on icy satellites. In *Satellites of Jupiter*, vol. 1, edited by Morrison D. and Matthews M. S. Tuscon, Arizona: The University of Arizona Press. pp. 340–378.
Grey I. D. S. and Burchell M. J. 2004. Hypervelocity impact craters in ammonia rich ice. *Icarus* 168:467–474.
Grey I. D. S., Burchell M. J., and Shrine N. R. G. 2001. Laboratory investigations of the temperature dependence of hypervelocity impact cratering in ice. *Advances in Space Research* 28:1527–1532.
Grey I. D., Burchell M. J., and Shrine N. R. G. 2002. Scaling of hypervelocity impact craters in ice with impact angle. *Journal of Geophysical Research: Planets* 107:5076.
Grieve R. A. F. 1987. Terrestrial impact structures. *Annual Review of Earth Planetary Sciences* 15:245–270.
Hartmann W. K. 1977. Relative crater production rates on planets. *Icarus* 31:260–276.
Hayne P. O., Hendrix A., Sefton-Nash E., Siegler M. A., Lucey P. G., Retherford K. D., and Paige D. A. 2015. Evidence for exposed water ice in the Moon's south polar regions from Lunar Reconnaissance Orbiter ultraviolet albedo and temperature measurements. *Icarus* 255:58–69.
Head J. W. 1976. The significance of substrate characteristics in determining the morphology and morphometry of lunar craters. Proceedings, 7th Lunar Science Conference. pp. 2913–2929.
Holsapple K. A. and Schmidt R. M. 1982. On the scaling of crater dimensions 2. Impact processes. *Journal of Geophysical Research* 87:1849–1870.
Hoppa G. V., Tufts B. R., Greenberg R., and Geissler P. E. 1999. Formation of cycloidal features on Europa. *Science* 285:1899–1902.

Ivanov M. A., Prockter L. M., and Dalton B. 2011. Landforms of Europa and selection of landing sites. *Advances in Space Research* 48:661–677.

Kadono T. and Fujiwara A. 1996. Observation of expanding vapour cloud generated by hypervelocity impact. *Journal of Geophysical Research: Planets* 101:26,097–26,109.

Kenkmann T., Jahn A., Scherler D., and Ivanov B. A. 2005. Structure and formation of a central uplift: A case study at the Upheaval Dome impact crater, Utah. *Geological Society of America Special Papers* 384:85–115.

Leliwa-Kopystynski J., Burchell M. J., and Lowen D. 2008. Impact cratering and break-up of the small bodies of the solar system. *Icarus* 195:817–826.

Lucchitta B. K. and Soderblom L. A. 1982. The geology of Europa. In *Satellites of Jupiter*, vol. 1, edited by Morrison D. and Matthews M. S. Tuscon, Arizona: The University of Arizona Press. pp. 521–555.

Melosh H. J. 1989. *Impact cratering: A geologic process. Research supported by NASA*. New York: Oxford University Press. 253 p.

Michel Y., Chevalier J. M., Durin C., Espinosa C., Malaise F., and Barrau J. J. 2006. Hypervelocity impacts on thin brittle targets: Experimental data and SPH simulations. *International Journal of Impact Engineering* 33:441–451.

Miljkovic K., Mason N. J., and Zarnecki J. C. 2011. Ejecta fragmentation in impacts into gypsum and water ice. *Icarus* 214:739–747.

Moore J. M., Asphaug E., Belton M. J., Bierhaus B., Breneman H. H., Brooks S. M., and Williams K. K. 2001. Impact features on Europa: Results of the Galileo Europa Mission (GEM). *Icarus* 151:93–111.

Pappalardo R. T., Belton M. J. S., Breneman H. H., Carr M. H., Chapman C. R., Collins G. C., and Williams K. K. 1999. Does Europa have a subsurface ocean? Evaluation of the geological evidence. *Journal of Geophysical Research: Planets* 104:24,015–24,055.

Pierazzo E. and Melosh H. J. 1999. Hydrocode modeling of Chicxulub as an oblique impact event. *Earth and Planetary Science Letters* 165(2):163–176.

Pierazzo E. and Melosh H. J. 2000. Understanding oblique impacts from experiments, modeling and experiments. *Annual Review of Earth and Planetary Sciences* 28:141–167.

Pike R. J. 1980. Control of crater morphology by gravity and target type-Mars, Earth, Moon. Proceedings, 11th Lunar and Planetary Science Conference. pp. 2159–2189.

Prockter L. M. 2005. Ice in the solar system. *Johns Hopkins APL Technical Digest* 26:175–188.

Ross M. N. and Schubert G. 1987. Tidal heating in an internal ocean model of Europa. *Nature* 325:133–134.

Schenk P. M. 1993. Central pit and dome craters: Exposing the interiors of Ganymede and Callisto. *Journal of Geophysical Research: Planets* 98:7475–7498.

Schenk P. M. and McKinnon W. B. 1989. Fault offsets and lateral crustal movement on Europa: Evidence for a mobile ice shell. *Icarus* 79:75–100.

Schenk P. M. and Turtle E. P. 2009. Europa's impact craters: Probes of the icy shell. In *Europa*, edited by Pappalardo R. T., McKinnon W. B., and Khurana K. Tucson, Arizon: The University of Arizona Press. pp. 181–198.

Senft L. E. and Stewart S. T. 2008. Impact crater formation in icy layered terrains on Mars. *Meteoritics & Planetary Science* 43:1993–2013.

Shrine N. R., Burchell M. J., and Grey I. D. 2002. Velocity scaling of impact craters in water ice over the range 1 to 7.3 km s^{-1}. *Icarus* 155:475–485.

Squyres S. W., Reynolds R. T., Cassen P. M., and Peale S. T. 1983. Liquid water and active resurfacing on Europa. *Nature* 301:225–226.

Stickle A. M. and Schultz P. H. 2013. Investigating pressure magnitudes at depth for oblique impacts into layered targets: Applications to terrestrial impacts in sedimentary targets. *Meteoritics & Planetary Science* 48:1638–1650.

Tanaka K. L. and Scott D. H. 1987. Geologic map of the polar regions of Mars. The US Geological Survey IMAP 1802.

Turtle E. P. and Pierazzo E. 2001. Thickness of a Europan ice shell from impact crater simulations. *Science* 294:1326–1328.

Walker C. C. and Schmidt B. E. 2015. Ice collapse over trapped water bodies on Enceladus and Europa. *Geophysical Research Letters* 42:712–719.

Wilcox B. B., Robinson M. S., Thomas P. C., and Hawkes B. R. 2005. Constraints on the depth and variability of the lunar regolith. *Meteoritics & Planetary Science* 40:695–710.

Wood C. A., Head J. W., and Cintala M. J. 1978. Interior morphology of fresh Martian craters—The effects of target characteristics. Proceeding, 9th Lunar and Planetary Science Conference. pp. 3691–3709.

Wünnemann K., Morgan J. V., and Jödicke H. 2005. Is Ries crater typical for its size? An analysis based upon old and new geophysical data and numerical modeling. *Geological Society of America Special Papers* 384:67–83.

Zahnle K., Schenk P., Levison H., and Dones L. 2003. Cratering rates in the outer solar system. *Icarus* 163:263–289.